Microsc. Microanal. 12, 85–91, 2006
DOI: 10.1017/S1431927606060120

Microscopy AND Microanalysis

Misorientation Mapping for Visualization of Plastic Deformation via Electron Back-Scattered Diffraction

L.N. Brewer,* M.A. Othon, L.M. Young, and T.M. Angeliu

General Electric Global Research Center, One Research Circle, Niskayuna, NY 12309, USA

Abstract: The ability to map plastic deformation around high strain gradient microstructural features is central in studying phenomena such as fatigue and stress corrosion cracking. A method for the visualization of plastic deformation in electron back-scattered diffraction (EBSD) data has been developed and is described in this article. This technique is based on mapping the intragrain misorientation in polycrystalline metals. The algorithm maps the scalar misorientation between a local minimum misorientation reference pixel and every other pixel within an individual grain. A map around the corner of a Vickers indentation in 304 stainless steel was used as a test case. Several algorithms for EBSD mapping were then applied to the deformation distributions around air fatigue and stress corrosion cracks in 304 stainless steel. Using this technique, clear visualization of a deformation zone around high strain gradient microstructural features (crack tips, indentations, etc.) is possible with standard EBSD data.

Key words: EBSD, plasticity, fracture, electron diffraction, misorientation

Introduction

Understanding the microstructural distribution of strain in a structural material is key to controlling the overall deformation at the macroscale. The microstructural distribution of strain is difficult to characterize because of the small-length scales involved. Many techniques that are amenable to the measurement of elastic and plastic strain (e.g., traditional X-ray residual stress, neutron diffraction) do not possess the spatial resolution required to make these measurements on the microstructural length scale (1–10 μm). However, recent advancements in capillary and synchrotron X-ray diffraction techniques (e.g., Margulies et al., 2001; Ice & Larson, 2004) have begun to allow this sort of investigation. Electron back-scattered diffraction (EBSD) (Wilkinson et al., 1993; Randle et al., 1996; Hu et al., 2000; King et al., 2000; Mino et al., 2000; Sun et al., 2000; Tucker et al., 2000; Li et al., 2002; El Dasher et al., 2003; Field et al., 2003, 2005; Kamaya et al., 2005) and related techniques, such as electron channeling contrast imaging (ECCI) (Gerberich et al., 1990; Wilkinson et al., 1996; Ahmed et al., 1999), have been used to map plastic deformation or strain at both macrostructural and microstructural levels. On the macroscale, EBSD combined with mechanical testing has been used successfully to measure plastic strain as a function of distance from a weld in stainless steels (Angeliu et al., 1999) and through tubes and around intergranular cracks in Ni-based alloys (Lehockey et al., 2000). EBSD has been explored as a means to map plastic deformation at a microstructural length scale both by monitoring the change in pattern quality (Wilkinson et al., 1993) and by monitoring the change in intragranular crystal orientation (Orsund et al., 1989; Wright, 1993; King et al., 2000). However, combining high spatial resolution with the strain sensitivity needed for characterizing the steep strain gradient ahead of a crack tip has been difficult. The clear visualization of deformation or strain has been challenging even at a qualitative level, with many methods giving deformation maps of varying interpretability. In this article, we discuss the use of an algorithm for visualizing plastic deformation at the micron-length scale. In particular, we will apply these methods to microstructures with potentially large plastic strain gradients, for example, indentations and crack tips. We first describe the application of a modified algorithm to a test measurement on austenitic 304 stainless steel. We then describe the application of this method to stress corrosion cracking (SCC) in this material.

Received April 14, 2005; accepted August 31, 2005
**Corresponding author*. E-mail: lnbrewe@sandia.gov
L.N. Brewer is now at Sandia National Laboratories, Albuquerque, New Mexico.

Materials and Methods

An initial test specimen was prepared by polishing a piece of 304 stainless steel to a 1-μm finish, followed by vibratory polishing with colloidal (50 nm) silica. Vickers indentations using a series of loads up to 1 kg were applied such that the

corner of a given indentation was inside a particularly large grain.

Orientation mapping was performed using standard EBSD mapping techniques with a commercial SEM (CamScan CS44, tungsten filament, thermionic emission) operating at 20 keV, commercial software (HKL Inc. Channel 5), and a CCD camera combined with a Hamamatsu Argus image analyzer. For the case of the indentation, scans of 120×120 steps of 0.25 μm in a beam scan mode were made on the sample surface. Patterns using 4–6 bands were automatically indexed using FCC iron (Fm–3m) as the phase at a rate of about six patterns per second.

Two compact tension (CT) specimens were prepared from sensitized 304 stainless steel. One specimen was fatigue precracked in room temperature air and then held at constant load (22 MPa • $m^{1/2}$) for 20 h at 288°C in argon. A second specimen was fatigue precracked in room temperature air and then loaded to 30 MPa • $m^{1/2}$ into an autoclave at 288°C and 10.3 MPa with deionized water with an added 2000 ppb oxygen for a total of 2113 h. The samples were removed from tension, sectioned parallel to the CT specimen surface, and polished to a 1-μm finish with a final vibratory polish with colloidal silica. Orientation mapping was performed using the same general techniques and conditions as above. EBSD scans of 400×400, 1-μm steps in a stage scan mode were made around the crack tips from both the CT specimen surface and the midplane of each specimen. No noise reduction was used on the data collected in these maps.

The misorientation mapping algorithm was written to map the internal rotation within a given grain due to plastic deformation and to map all of these "single grain maps" onto the same microstructural visualization. The general steps are as follows:

1. Establish grains in microstructure.
   a. Locate grain boundaries using standard misorientation calculations (10° threshold).
   b. Assign each pixel in the map to a grain.
2. Determine the reference pixel for an individual grain.
   a. Calculate misorientation for all nine-pixel clusters within a given grain, disregarding boundary pixels.
   b. Choose the cluster with least misorientation as reference (minimum distortion).
3. Calculate and map the misorientation.
   a. For a given grain, calculate the misorientation between each pixel and the reference pixel.
   b. Map this misorientation for each pixel using a color table.

Results

Different representations of the same data set revealed strikingly different information about the deformation in the indented grain. A Euler angle map (orientation map; Fig. 1a) clearly shows the grains in the microstructure and the presence of the indentation (lack of indexed pixels), but shows no sensitivity to the plastic deformation field associated with the indentation. A pattern quality map (Fig. 1b) displays subtle but perhaps confusing variations in contrast around the indentation corner. In particular, a scratch on the sample surface is a visible artifact in this map. The "pattern quality" map in Figure 1b is actually a map of band contrast, which is defined as the jump in contrast between the edge of the band and the adjacent background in the EBSD pattern. A map of the "low-angle grain boundaries" (GB map; Fig. 1c) demonstrates the effect of deformation more directly. Grain boundaries are defined by the scalar degree of misorientation, θ, between any two adjacent pixels. The high-angle boundaries (black, $\theta > 10°$) are located as expected from the Euler angle map. The low-angle boundaries (red, $2° < \theta < 10°$), can represent walls or arrays of dislocations and display local gradients in misorientation. A much higher density of low-angle boundaries is observed along the edge of the indentation than in the interior of the grain, with the scratch again being visible in the map. A clear deformation pattern in the middle of the grain is not visible.

Figure 1d,e shows maps based on other methods for mapping deformation. Figure 1d is a map of average internal misorientation (AMIS) value (Sutliff, 1999) as plotted in the HKL Channel 5 software. At this subgrain-length scale, an AMIS map does not capture the misorientation gradient that is of central interest for features such as indentations and crack tips. Figure 1e is a map of local, cluster misorientation (misorientation among a cluster of nine pixels). This method of visualization gives results similar to the boundary maps in Figure 1c, with a higher density of misorientation clusters at the edge of the indentation, but with little definition of the deformation field in the center of the grain. However, the map in Figure 1e is actually an intermediate step in the calculation of the intragrain misorientation map in Figure 1f.

Direct mapping of the intragrain misorientation clearly shows the deformation field associated with the indentation (Fig. 1f). Within each grain, the misorientation between the reference pixel and every other pixel is plotted using a color map from blue (0°) to red (10°). Small misorientations (0.3–0.5°, blue) represent small amounts of intragrain misorientation/lattice rotation and therefore little deformation. Large misorientations (e.g., 10°, red) represent large amounts of intragrain misorientation/lattice rotation and therefore large deformation. The limit of 10° was chosen as a reference because it is commonly used to denote the lower bound for a high-angle grain boundary. The misorientation map of the indent captured both the deformation field along the edge of the indentation and the deformation zone extending into the grain from the corner of the indentation. In addition, the scratch was visible as in Figure 1b,c.

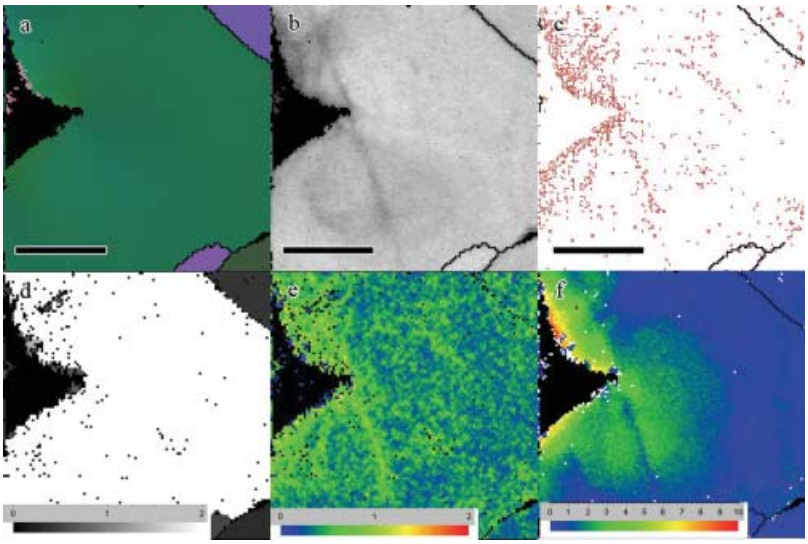

Figure 1. Different mapping algorithms applied to a data set from a small Vickers indentation on 304 stainless steel. Scale bar on all figures is 10 μm. **a:** Euler angle map (each color represents one grain orientation). **b:** Band contrast map (gray scales represent the "quality" of the EBSD pattern). **c:** Grain boundary map (black lines are high angle [$\theta > 10°$] boundaries, red lines are low angle [$2° < \theta < 10°$] boundaries). **d:** Average internal misorientation map (see legend, 0–2° average misorientation). **e:** Pixel cluster misorientation map (see legend, 0–2° cluster misorientation). **f:** Misorientation map (rainbow scale: blue represents 0° misorientation from the reference pixel, red represents 10° misorientation from the reference pixel).

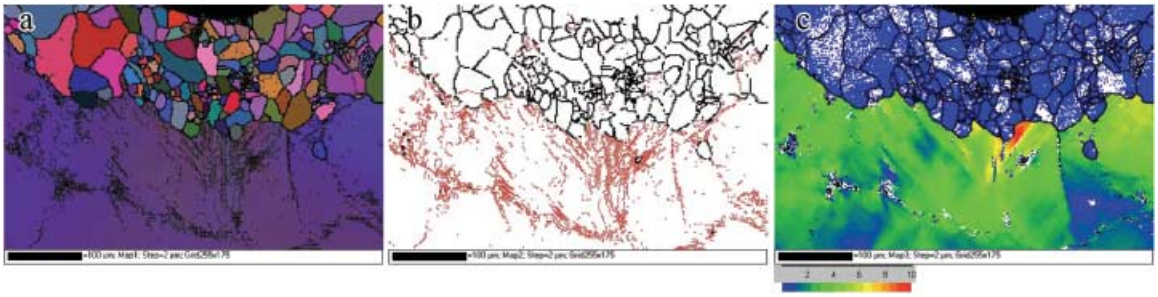

Figure 2. EBSD maps of partial recrystallization of indentation in single crystal Ni-based alloy. **a:** Euler angle map. **b:** Grain boundary map (black lines are high angle [$\theta > 10°$] boundaries, red lines are low angle [$2° < \theta < 10°$] boundaries). **c:** Misorientation map (rainbow scale: blue represents 0° misorientation from reference, red represents 10° misorientation from reference). White spots in recrystallized regions are artifacts for this particular data set.

The effectiveness of this approach was also demonstrated for a recrystallization front in an FCC single crystal (Fig. 2). The Euler angle map (Fig. 2a) clearly showed the single crystal itself along with small grains above the front (cross-sectional view). The GB map (Fig. 2b) did display a strong difference in low-angle boundary (red lines) density between the recrystallized grains on the upper surface versus the deformed region below the front. The boundary between recrystallized (blue) grains and deformed material ahead of the recrystallization front (blue to red) was made even clearer by the misorientation map (Fig. 2c). In addition, the misorientation map showed deformation gradient patterns in a V shape indicative of the single crystal slip in the deformed region.

EBSD maps of the ambient-environment crack tip show a strong deformation zone extending several grains from the tip. The crack tip is apparently blunted, which may be due to modest creep deformation during testing. A map of the high-

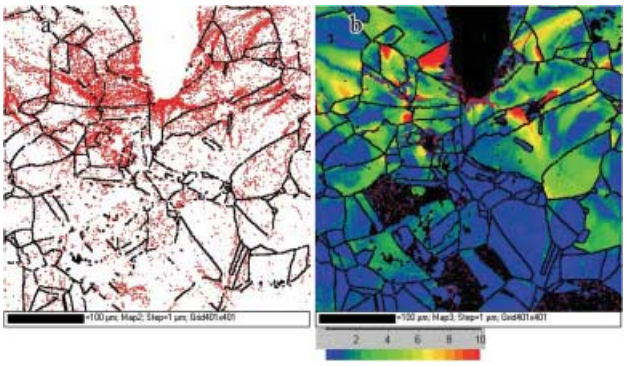

Figure 3. EBSD maps from a region around an air fatigue crack tip in 304 stainless steel. Scale bar is 100 μm. **a:** Grain boundary map (black lines are high angle [$\theta > 10°$] boundaries, red lines are low angle [$2° < \theta < 10°$] boundaries). **b:** Misorientation map (rainbow scale: blue represents 0° misorientation from reference, red represents $\geq$10° misorientation from reference).

and low-angle grain boundaries (Fig. 3a) displays a lateral spreading of deformation from the tip. The corresponding misorientation map (Fig. 3b) shows even further extension of the deformation zone around the crack tip. In both cases, the maps demonstrate a steep gradient in plastic deformation surrounding the crack tip. The collection of grains with noticeable deformation takes the kidney-bean shape that would be expected from a mode I crack in continuum fracture mechanics. Similar deformation/misorientation distributions were noticed for all parallel sections taken from the same compact tension specimen. An almost completely red grain appears to the bottom right of the crack tip. This grain has this uniform red color because the internal misorientation from the reference pixel exceeded 10°. It is important to note that the *total* misorientation between two, nonadjacent pixels in a grain can exceed 10° without being classified as a high-angle grain boundary (HAGB). The 10° definition of a HAGB is only for adjacent pixels.

EBSD maps of the fatigue portion of the stress corrosion crack (SCC) show similar behavior to the air fatigue crack sample (Fig. 4a). The GB map does not display the deformation clearly and unfortunately detects scratches on the sample surface. The misorientation map (Fig. 4b) clearly shows the deformation wake along the crack and has deformation features that can be clearly matched to strain contrast in the matching BSE image (Fig. 4c). The matching of these features is important because it supports the validity of features mapped by the misorientation algorithm. It is interesting to note that the misorientation map shows deformed grains along the wake of the fatigue crack as would be expected from continuum fracture mechanics.

EBSD maps of the stress corrosion crack (SCC) region showed varying amounts of deformation (Figs. 5 and 6). In region 1 (Fig. 5), little deformation is observed around the crack and its tip. The grain boundary map (Fig. 5a) shows almost as many small angle boundaries in grains far away from the crack as near the crack, although a somewhat higher density of low-angle boundaries can be seen running along the crack plane itself. The misorientation map (Fig. 5b) also displays limited deformation, confined primarily to the intercept between the SCC tip and triple junctions within the microstructure. However, in SCC region 2 of the sample (Fig. 6), the SCC traveled along the grain boundary until it reached a triple point boundary. At this point one of the grains is apparently absorbing more deformation than the neighboring grains. It may also be that the automated choice of reference pixel was not physically the best, as is discussed below. A reference pixel taken near the center of the grain might show a fairly deformation-free grain with deformation right at the triple junction. The grain boundary map (Fig. 6a) does not capture this deformation well, but the misorientation map (Fig. 6b) clearly displays the deformation in this large grain and in the other grains surrounding the intersection of the triple point boundary and the SCC.

Discussion

The mapping of intragrain misorientation has advantages and disadvantages over other analysis approaches for the visualization of localized plastic deformation. Maps of overall orientation (such as Euler maps) are not particularly sensitive to deformation, but can show deformation and the associated changes in orientation within large grains. EBSD pattern quality maps can effectively map plastic deformation and have even been used to do so quantitatively using careful, Fourier transform analysis of EBSD patterns (Wilkinson & Dingley, 1991). However, the use of band contrast in the present study was not sufficient to reliably capture the deformation gradients in the indented and cracked samples. Simple grain boundary mapping (using a threshold misorientation to define a grain boundary) did show some utility as a mapping algorithm in this work, but it did not provide the same ease of interpretation as intragrain misorientation mapping algorithm. Work by Tucker et al. (2000) also pointed out the inability of grain boundary mapping to visualize crack wake and plastic zone features for fatigue cracks in super alloys (grain boundary maps are termed "misorientation" maps in that paper). However, Lehockey et al. (2000) did use low angle ($<5°$) grain boundary maps to observe crack wakes in alloy 600. Previous work by King et al. (2000) has demonstrated the use of intragrain misorientation mapping at the microstructural-length scale, particularly for shear banding in single crystals. One disadvantage of misorientation mapping techniques is their lack of connection to more quantitative measures of deformation such as strain, strain gradient, or dislocation density. Further analysis of grain boundary maps or misorientation gradient maps can be used to connect the observed deformation with the local density of geometrically necessary dislocations (GNDs). The work by Tucker et al. points out that simple dislocation models can be used to estimate local GND densities from grain boundary maps. An elegant study, by Sun et al. (2000), developed the connection between misorientation gradient (related to grain boundary mapping), the Nye curvature tensor, and geometrically necessary dislocation density, and then applied these analytics to model experiments on Al bicrystals. This GND mapping approach has been further applied to microstructures by El Dasher et al. (2003) and most recently by Field et al. (2005).

When using a misorientation mapping approach for visualizing plastic deformation, the choice of the reference misorientation can substantially affect the resulting map. Including the current work, there are at least four approaches for selecting a reference pixel for misorientation maps. The earliest paper by Wright (1993) uses the simple mean orientation as the reference pixel and then plots the misorientation for every pixel with respect to this mean orientation. The second approach is to find a median orientation by a regression analysis as described by King et al. (2000). The Kamaya approach is to find the pixel that has

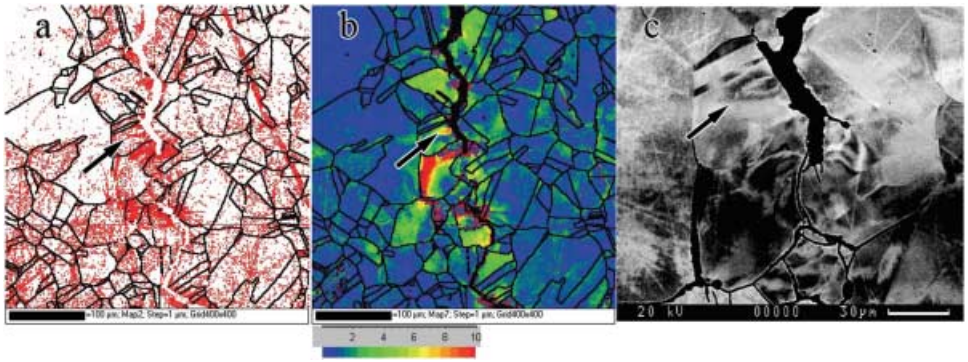

Figure 4. Fatigue portion of stress corrosion crack (SCC) in 304 stainless steel. Scale bar is 100 μm. **a:** Grain boundary map (black lines are high angle [$\theta > 10°$] boundaries, red lines are low angle [$2° < \theta < 10°$] boundaries). **b:** Misorientation map (rainbow scale: blue represents 0° misorientation from reference, red represents 10° misorientation from reference). **c:** Back-scattered electron image of same region. Note that same contrast feature is marked with an arrow in each image/map.

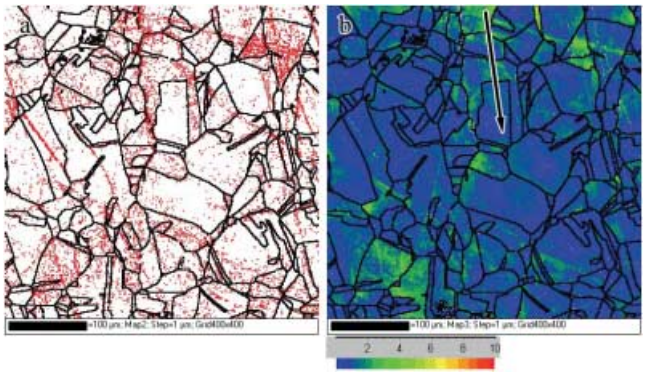

Figure 5. Maps of SCC from the first region in 304 stainless steel sample. Crack inside of ellipse in both images. Scale bar is 100 μm. **a:** Grain boundary map (black lines are high angle [$\theta > 10°$] boundaries, red lines are low angle [$2° < \theta < 10°$] boundaries). **b:** Misorientation map (rainbow scale: blue represents 0° misorientation from reference, red represents 10° misorientation from reference).

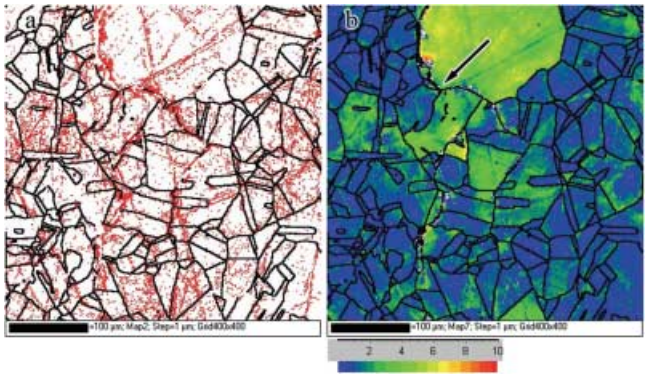

Figure 6. Maps of SCC from second region in 304 stainless steel sample. **a:** Grain boundary map (black lines are high angle [$\theta > 10°$] boundaries, red lines are low angle [$2° < \theta < 10°$] boundaries). Scale bar is 100 μm. **b:** Misorientation map (rainbow scale: blue represents 0° misorientation from reference, red represents 10° misorientation from reference). White arrows show direction of crack propagation. Black arrow indicates triple junction. Scale bar is 100 μm.

the smallest total misorientation as calculated by summing the misorientations between any given pixel and all of the other pixels in a grain (Kamaya et al., 2005). The current approach is to calculate the summed misorientation for any given pixel and all of its nearest neighbors. The arithmetic mean approach is simple to implement but does not have a strong connection to the intragrain distribution of deformation. The median approach works well for single crystals, but again has a weaker connection to the internal deformation of a given grain in a polycrystal. The Kamaya approach and the current one are limits of each other. The current approach attempts to find the flattest local portion of a grain whereas the Kamaya approach expands the definition of a local kernel to include the entire grain. The current approach is helpful in grains that possess relatively flat regions (not deformed) and deformed regions (e.g., a crack tip), but this approach can become more ambiguous for grains that have very complex deformation patterns, as there are likely to be several "flat" regions in the crystal. This ambiguity in local kernel choice might lead to a less than ideal assignment of the deformed regions of a given grain.

The connection between the misorientation mapping in this algorithm and the mapping of strain is proportional, but not well understood. The data in this study are not representative of elastic strain fields in the sample, particularly given the much smaller magnitude of the elastic strains. Measurement of elastic strain would require precise measurement of the lattice parameter and is currently beyond the capability of standard EBSD measurements. In addition,

it is likely that the elastic strain fields might experience significant relaxation at the surface (approximately the top 100 nm) of the specimen being probed. Instead, the misorientation maps are measuring the geometric bending of the crystalline lattice and are therefore measurements of geometric plastic deformation at the microstructural level. The sensitivity limit of this EBSD technique is not well established. The related average intragrain misorientation measurements of Sutliff (1999) demonstrated sensitivity for calibration samples that had been macroscopically strained to 1%, which is far greater than the traditional engineering definition of plastic strain of 0.2% in uniaxial tension. Likewise, Lehockey et al. (2000) observed a sensitivity of 1% strain for a calibration between plastic strain and average intragrain misorientation (termed *integrated angular misorientation density*) on alloy 600 specimens. From the diffraction standpoint, the noise floor for misorientation in a standard, calibrated EBSD instrument is approximately $\pm 0.5^\circ$ (Wilkinson, 2001). Additionally, this technique is not sensitive to strain gradients in three dimensions or to the density of statistically stored dislocations (Sun et al., 2000). At this point, it should be assumed that the misorientation mapping algorithm is capable of detecting lattice rotations that correspond to plastic strain fields and strain gradient regimes like those found at crack tips, but that it would not be capable of accurate measurement of plastic zone sizes.

A sense of this sensitivity can be gained by comparing the calculated plastic zone size with the measured deformation zone from the data in Figure 3. The plastic zone size for a mode I crack in a plane strain geometry is given by

$$r_y = \frac{1}{2\pi}\left(\frac{K}{\sigma_y}\right)^2 \tag{1}$$

where r_y is the plastic zone radius, K is the stress intensity factor, and σ_y is the yield strength of the material. The yield strength for the material in this test was measured to be approximately 186 MPa with the stress intensity of 22 MPa$\sqrt{\text{m}}$ as noted above. These numbers result in a plastic zone radius of about 2 mm. This plastic zone size is more than five times the field of view of Figure 3, and so it appears that this measurement is sensitive only to deformation that is much greater than the strain limit that defines the plastic zone size.

One of the benefits and challenges of this misorientation mapping technique is that it is sensitive to deformation on a grain-by-grain basis. In Figures 3b and 4b, deformation is clearly mapped around the crack tips and wakes in a manner that is reminiscent of continuum level elasto-plastic fracture mechanics predictions. It is clear, however, that the deformation is heterogeneously distributed among the grains surrounding the cracks. This deformation distribution should be expected, as the different orientations among these grains result in different levels of deformation because of plastic anisotropy. The ability to map these grain-by-grain deformation distributions will be helpful in understanding the local mechanics, but it will be challenging to connect with the understood continuum level mechanics. Future work will involve the comparison of model samples with both EBSD measurements and finite element calculations to examine deformation at this micro-length scale.

Finally, this is the first study to directly map plastic deformation of fatigue and stress corrosion cracks of sensitized 304 stainless steel. These limited data suggest that there is more plastic deformation during air fatigue than during SCC at 288°C. This observation could simply reflect the role of corrosion in making grain boundaries more susceptible to intergranular fracture and thus obviating the need for extensive plastic deformation to sustain SCC growth. The enhanced interaction of SCCs with triple junctions may have similarities to the observations by Lehockey et al. (2000) in alloy 600. More analysis is required, but the visualization of plastic deformation using EBSD patterns is a very promising method to advance our understanding of the mechanisms behind SCC.

Conclusion

An algorithm has been developed for mapping misorientation and plastic deformation in metals using EBSD techniques. This algorithm can be used on standard EBSD data sets. Maps from indented, fatigue cracked, and stress corrosion cracked specimens demonstrated the utility of this misorientation mapping algorithm to the visualization of plastic deformation, particularly for microstructures with large plastic gradients. Future work will examine both the application of this method on carefully controlled deformation experiments and the further connection of misorientation to actual plastic strain.

Acknowledgments

We would like to acknowledge the support of R. Horn at GE Nuclear Energy for the development of this work. Additionally, the authors thank A. Barbuto, R. Schnoor, and G. Catlin for assistance in preparing the test samples and J. Sutliff and K. Mehnert of HKL Technologies for helpful discussions and programming support. The authors also thank M. Gigliotti and C. Hardwicke for providing the recrystallization front data set and B. Boyce and J.R. Michael for reviewing the manuscript. Thanks to S. Wright and A. Wilkinson for helpful discussion on the manuscript.

References

Ahmed, J., Wilkinson, A.J. & Roberts, S.G. (1999). Study of dislocation structures near fatigue cracks using electron channeling contrast imaging technique (ECCI). *J Microsc* **195**, 197–203.

Angeliu, T.M., Andresen, P.L., Hall, E., Sutliff, J.A., Sitzman, S. & Horn, R.M. (1999). Intergranular stress corrosion cracking of unsensitized stainless steels in BWR environments. In *Proceedings of the Ninth International Symposium on Environmental Degradation of Materials in Nuclear Power Systems-Water Reactors*, pp. 311–317. Newport Beach, CA.

El Dasher, B.S., Adams, B.L. & Rollett, A.D. (2003). Viewpoint: Experimental recovery of geometrically necessary dislocation density in polycrystals. *Scripta Mater* **48**, 141–145.

Field, D.P., Trivedi, P.B., Wright, S.I. & Kumar, M. (2005). Analysis of local orientation gradients in deformed single crystals. *Ultramicroscopy* **103**, 33–39.

Field, D.P., Wright, S.I. & Trivedi, P. (2003). Microtextural analysis of grain fragmentation in aluminum. *Mater Sci Forum* **426–432**, 3739–3744.

Gerberich, W.W., Davidson, D.L. & Kaczorowski, M. (1990). Experimental and theoretical strain distributions for stationary and growing cracks. *J Mech Phys Solids* **38**, 87–113.

Hu, Y.M., Floer, W., Krupp, U. & Christ, H.J. (2000). Microstructurally short fatigue crack initiation and growth in Ti-6.8Mo-4.5Fe-1.5Al. *Mater Sci Eng A* **278**, 170–180.

Ice, G.E. & Larson, B.C. (2004). Three-dimensional X-ray structural microscopy using polychromatic microbeams. *MRS Bull* **29**, 170–176.

Kamaya, M., Wilkinson, A.J. & Titchmarsh, J.M. (2005). Measurement of plastic strain of polycrystalline material by electron backscatter diffraction. *Nucl Eng Des* **235**, 713–725.

King, W.E., Stolken, J.S., Kumar, M. & Schwartz, A.J. (2000). Strategies for analyzing EBSD datasets. In *Electron Backscatter Diffraction in Materials Science*, Schwartz, A.J., Kumar, M. & Adams, B.L. (Eds.), pp. 153–169. New York: Kluwer Academic.

Lehockey, E.M., Lin, Y. & Lepik, O.E. (2000). Mapping residual plastic strain in materials using electron backscatter diffraction. In *Electron Backscatter Diffraction in Materials Science*, Schwartz, A.J., Kumar, M. & Adams, B.L. (Eds.), pp. 247–264. New York: Kluwer Academic.

Li, B.L., Godfrey, A. & Liu, Q. (2002). Investigation of macroscopic grain sub-division of an IF-steel during cold rolling. *Mater Sci Forum* **408–412**, 1185–1190.

Margulies, L., Winther, G. & Poulsen, H.F. (2001). In situ measurement of grain rotation during deformation of polycrystals. *Science* **291**, 2392–2394.

Mino, K., Fukuoka, C. & Yoshizawa, H. (2000). Evolution of intragranular misorientation during plastic deformation. *J Jpn Inst Metals* **64**, 50–55.

Orsund, R., Njelen, J. & Nes, E. (1989). Local lattice curvature and deformation heterogeneities in heavily deformed aluminum. *Scripta Metall* **23**, 1193–1198.

Randle, V., Hansen, N. & Juul Jensen, D. (1996). The deformation behaviour of grain boundary regions in polycrystalline aluminum. *Phil Mag A* **73**, 265–282.

Sun, S., Adams, B.L. & King, W.E. (2000). Observations of lattice curvature near the interface of a deformed aluminium bicrystal. *Phil Mag A* **80**, 9–25.

Sutliff, J.A. (1999). An investigation of plastic strain in copper by automated EBSP. In *Microscopy and Microanalysis*. Portland, Oregon: Springer Verlag.

Tucker, A.T., Wilkinson, A.J., Henderson, M.B., Ubhi, H.S. & Martin, J.W. (2000). Measurement of fatigue crack plastic zones in fine grain materials using electron backscattered diffraction. *Mater Sci Technol* **16**, 427–430.

Wilkinson, A.J. (2001). A new method for determining small misorientations from electron back scatter diffraction patterns. *Scripta Mater* **44**, 2379–2385.

Wilkinson, A.J. & Dingley, D.J. (1991). Quantitative deformation studies using electron back scatter patterns. *Acta Metall* **39**, 3047–3055.

Wilkinson, A.J., Gonzalez, G. & Dingley, D.J. (1993). The measurement of local plastic deformation in a metal–matrix composite by electron back-scatter patterns. *J Micros* **169**, 255–261.

Wilkinson, A.J., Henderson, M.B. & Martin, J.W. (1996). Examination of fatigue crack plastic zones using scanning-electron-microscope-based electron diffraction techniques. *Phil Mag Lett* **74**, 145–151.

Wright, S.I. (1993). A review of automated orientation imaging microscopy (OIM). *J Comput Assist Microsc* **5**, 207–221.